An Experimental and Numerical Study of Deformation Behavior of Steels in Biaxial Tensile Tests

Dilip Banerjee, Mark Iadicola, Adam Creuziger, and Timothy Foecke
Material Measurement Laboratory
National Institute of Standards and Technology (NIST)
Gaithersburg, MD 20899

Keywords: Cruciform, biaxial tensile tests, finite element analysis

Abstract

Lightweighting materials are increasingly being used by automotive companies as sheet metal components to meet fuel economy targets by the year 2025. Consequently, accurate material model data need to be developed by applying biaxial strain paths with cross-shaped specimens, since traditional uniaxial stress-strain data cannot capture the deformation behavior in complex forming operations.

This paper discusses the development of finite element models and verification of these models against experimental measurements. Such verification is the first step in developing procedures for making an optimum cross-shaped specimen design. Computed results of deformation, strain profile, and von Mises plastic strain in two different specimens agree with experimentally measured values along critical paths in the specimens. In addition, simulated results predict correctly the eventual failure location in the samples. Detailed analyses also suggest that specimen thickness has an influence on the eventual mode of failure. Further studies are being conducted to confirm this conclusion.

1. Introduction

Automotive companies are actively interested in the increased use of advanced lightweighting materials such as advanced high strength steels (AHSS), aluminum alloys, and fiber reinforced plastics as sheet metal components to meet planned fuel economy targets by the year 2025. However, accurate material models are needed for wider adoption of these materials in the automotive industry. These material models need to be validated by using complex strain paths and plastic strains as typically encountered during the metal forming operations. Traditional uniaxial stress-strain data are not sufficient to capture the deformation behavior during these complex forming operations. Such data are often developed using bilinear strain paths using cross-shaped biaxial specimens (i.e., cruciform) [1, 2, 3, 4].

An important issue for successful cruciform testing is the specimen design itself. Over the years, researchers have used a wide variety of designs [5, 6, 7, 8, 9, 10, 14]. Generally the design of the specimens optimizes the following goals: (a) Both strain uniformity and eventual failure in the biaxially loaded gauge area, (b) Reduction of stress concentration outside of the gauge area, (c) Minimization of shear strains in the gauge area, (d) Similar behavior during repeat tests.

A goal of the present research is to develop cruciform designs that achieve these objectives for a wide variety of materials. Traditional finite element analysis (FEA) in conjunction with an optimization software can be used to conduct a systematic study to develop an optimum design of cruciform specimens that fulfils the above objectives. However, the first step toward achieving this goal is to verify the FEA models against detailed and careful experimental measurements. Additionally, if an appropriate constitutive law of the material is known, the FEA analysis can be used to determine stresses in the gauge section of the specimen, which are often difficult or impossible to measure directly by experiments.

Recently, the NIST Center for Automotive Lightweighting (NCAL) [11] has developed a state of the art biaxial testing facility that can (a) impart large biaxial strains on a cruciform sample using controlled nonlinear and non-monotonic strain paths without unloading the sample, (b) permit strain control and strain measurement using a combination of non-contacting 2D real-time and 3D post-processed Digital Image Correlation (DIC) systems, and (c) conduct X-ray diffraction for obtaining surface stress state in the gauge area of interest. In this work, only small portions of these capabilities are used.

The objective of the present paper is three-fold. The first goal is to develop finite element models of cruciform specimens and verify these models using careful experimental measurement of strain and displacement fields. Toward this end, an initial design of the cruciform specimen was chosen based on a literature review. The second goal is to provide insight into the plastic deformation behavior of the specimen design in the gauge area using both experimental and simulated results. The third goal is to develop capabilities for systematically comparing DIC measurement results with FEA computed data.

2. Cruciform Specimen Design and Biaxial/Uniaxial Tensile Tests

2.1 Cruciform Specimen Design

The inherent advantages of using the cruciform geometry for in-plane biaxial tests are that (a) the region of interest is far away from locations where boundary conditions are applied (contact or friction problems are not typically encountered) and (b) varying strain ratios can be applied along the arms of the specimen (e.g. equal biaxial strain evolving into plane strain). As mentioned earlier, the designs of the cruciform specimens vary widely. In most of the specimen designs, failure occurred outside the central gauge section of interest and at strains well below traditional forming limit strains. This is due to a combination of various factors, most notably stress and deformation concentrations at corners or near slits in the arms [12]. In some of these designs, the central gauge section is thinned down to achieve higher strain and possibly failure in the middle of the gauge section. This is a convenient starting point for specimen design although one would prefer using as-received sheets in the specimen design without altering thicknesses.

In this study, the specimen design follows that of Abu-Farha *et al.* [10], with the initial specimen being enlarged in all three directions to a thickness of 0.953 mm. Abu-Farha *et al.* [10] reported failure in the central region of the gauge section for heated specimens employing this geometry, but did not report results from any room temperature tests. This present specimen design is shown in Fig. 1. Cruciform samples were machined by water-jet with the X-axis aligned with the rolling direction of the sheet. One specimen was made of 9.525 mm (0.375 in) thick hot-rolled low carbon steel (hereinafter called "thick specimen"). The other specimen was made of 3.175 mm (0.125 in) thick cold-rolled AISI 1008 steel (hereinafter called "thin specimen"). This steel has much lower yield and ultimate tensile strength than the hot-rolled low carbon steel used for the thick specimen. Fig. 1 shows designed dimensions of the thick specimen. The thin specimen used a similar geometry except that it had a designed thickness of 0.749 mm (0.0295 in) in the center pocket (1.09 mm (0.043 in) of material was removed from top and bottom surfaces using electric discharge machining i.e., EDM) and that the fillet radius at the peripheral region of the central pocket was 0.397 mm (0.016 in).

2.2 Biaxial Tensile Tests

Biaxial loading was applied using four hydraulic actuators, which are controlled in orthogonal pairs [12]. Each of these actuators has 500 kN load capacity and has a ±50 mm displacement range from a reference distance of 640 mm between grip faces on the X or Y-axis. Details of the loading and in situ data acquisition using DIC system are described in [12]. In the present study, the biaxial tests were conducted using displacement control. An attempt was made to apply the same 0.004 mm/s displacement rate on both axes simultaneously. After fracture was observed, the displacement on both of the axes was stopped

before full separation of the test piece. Fig. 2 shows force-displacement curves in the X-direction for these two tests (note the force scale is substantially larger for the thick specimen). Similar curves were recorded for the Y-direction (not shown).

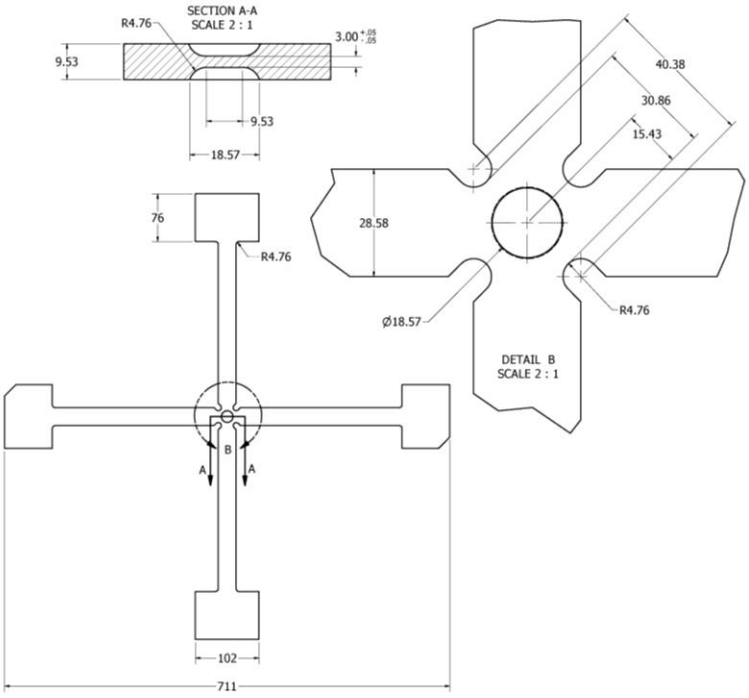

Fig. 1 Cruciform geometry used for the thick specimen (dimensions in mm).

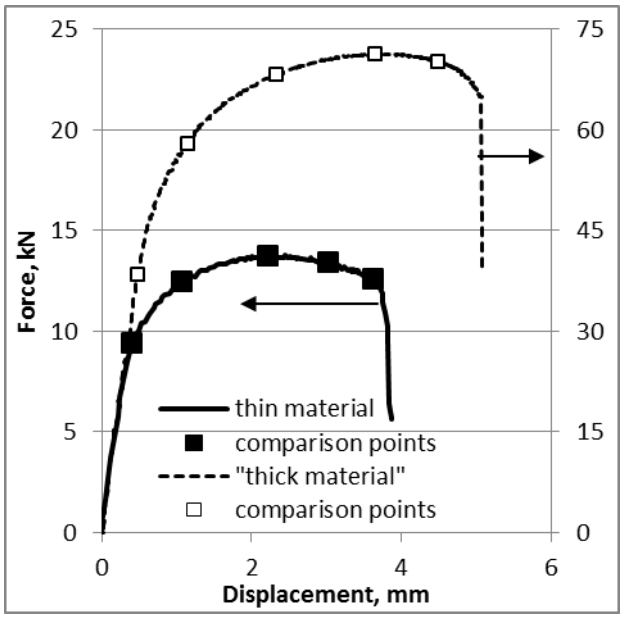

Fig. 2. Force-displacement curves for X-axis from cruciform specimens. Curves for Y-axis are similar and are not shown. Also shown points marked A through E, when DIC data along a diagonal path are extracted (see text).

The 3D displacement of top surface about the center of the cruciform specimen was measured with a stereo DIC system over a total field of view of approximately 70 mm x 65 mm. The system measures the surface U, V, and W displacements in the X, Y, and Z directions, respectively. Note that DIC requires a portion of the surface on which to correlate, thus the measurement points begin about 0.3 mm from the edges of the surfaces. Surface strains are calculated from the measured displacement fields. Note the following uncertainties in measurements: force +/- 0.025 kN; U, V, W displacements: (1.5, 1.5, and 2.5) μm respectively (thin specimen); U, V, W displacements: (3.0, 3.0, and 4.0) μm respectively (thick specimen).

Following the cruciform biaxial tensile tests, history-dependent U and V values at locations approximately 25 mm away from the central point were extracted for subsequent use in FEA simulation (discussed later). The displacement values were interpolated from the DIC field data at the FEA nodal coordinate values nearest to X=25 mm across the X-arm and nearest to Y=25 mm across the Y-arm (see displacement boundary locations in Fig. 3). Since symmetry was used in the model (discussed later), the same symmetry was applied to the sampling of the DIC data and only the average U values were used for the X-arm and similarly average V values for the Y-arm in the FEA model.

As stated earlier, cross-shaped specimens tend to concentrate strain in the corners between the arms, which leads to failure starting in the corners or premature failure in the gauge area. Any FEA model that will be used for specimen optimization must be able to capture the mechanical behavior in these corners. In order to compare the experimental and numerical results in these critical areas, displacement and strain data were extracted along a diagonal line (divided in 20 equal points) that bisects the region between the

central pocket and the reentrant radius at the meeting point of the X and Y arms (see "Path" in Fig. 3). This results in four sets of measured data, one from each corner area, for each sample. These data will be compared to the model predicted data along the same path. Note that these data were extracted at five specific times as shown in Fig. 2. The strain fields for the point of maximum force will also be compared. Uncertainties in strain measurement were: +/- 0.000450 m/m (in xx and yy) to +/- 0.000650 m/m (von Mises and zz) for thin specimen and +/-0.000400 m/m (in xx and yy) to +/- 0.000600 m/m (von Mises and zz) for thick specimen. Stress uncertainty varied from +/-0.45 MPa to +/-0.8 MPa.

2.3 Uniaxial Tensile Tests

Uniaxial tensile tests were performed for both steels in the rolling direction of the sheet. These tests were performed using the X-axis of the cruciform machine and the DIC system. The gauge section as designed has a nominally parallel length of 101.6 mm and width of 19.05 mm with radii of 50.8 mm to the 28.58 mm wide end-tabs. The same planer geometry was used for both thicknesses of material. The as-machined (by water-jet) widths and thicknesses were measured and used to calculate the initial cross-sectional area. Since the biaxial test and model will achieve strains beyond the uniform strain of a standard tensile test, it is necessary to either extrapolate the standard test data, or approximate the true-stress/true-strain relationship, to strains beyond uniform deformation. An approximation method was chosen that uses the DIC data sampled across the width of the specimen at the axial location of the eventual localized neck and failure. True axial strain was calculated as the average axial strain across the width for each point in time. The true stress was calculated as the applied end force divided by the current cross-sectional area at the same location and time. No correction for stress triaxiality was used. The resulting stress strain curves are shown in Fig. 4.The uniaxial test for the thin material used a constant displacement rate, which resulted in an undesirable increase in strain rate from approximately $8x10^{-5}$ s^{-1} before localization (maximum force) to $2x10^{-3}$ s^{-1} as the sample approached failure. In the thick material uniaxial test the displacement rate was reduced twice during the test (at approximately 0.26 and 0.49 true strain) to keep the average strain rate near $9x10^{-4}$ s^{-1}. Strain uncertainties varied from +/- 0.000400 m/m (in xx and yy) for the thin specimen to +/-0.000800 m/m (in xx and yy) for the thick specimen.

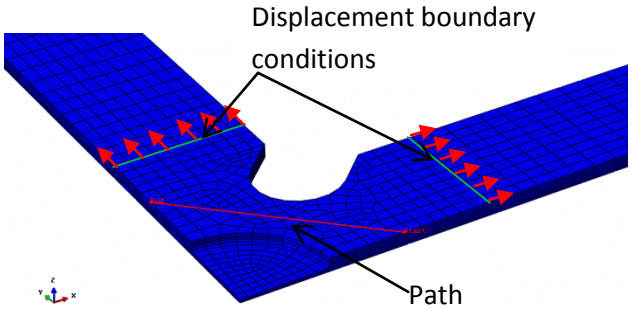

Fig. 3. A portion of the finite element mesh of the thin cruciform specimen. Also shown is the path in red color on which the FEA results are extracted for comparison with experimental measurements. Locations of axial displacement boundary conditions are also shown.

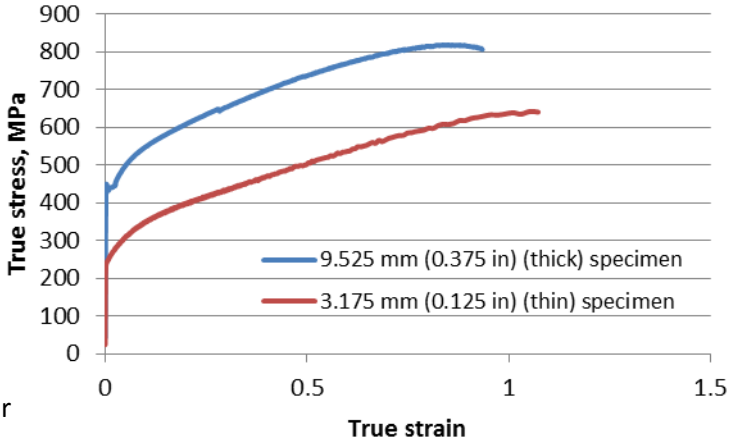

Fig. 4. True stress – true strain data obtained in uniaxial tensile tests.

3. Finite Element Modeling

A 3D finite element model of the cruciform specimens was developed using ABAQUS[1] software [13]. Constitutive material model data were obtained from experimental stress-strain measurements in uniaxial tension tests as shown in Fig. 3. Isotropic hardening is assumed in this study. Commonly used steel elastic properties were assumed for both materials, with a Young's modulus equal to 210 GPa and Poisson ratio of 0.3. A 1/8th symmetry FEA model was developed by taking advantage of the mirror symmetry in the specimen shape and loading. The solid model was developed in several parts. Each part was meshed individually using mapped meshing. 3D linear hexahedral elements (both regular and reduced integration elements e.g. C3D8 and C3D8R) were used for meshing. Note that C3D8R has one Gauss (integration) point per element located at the centroid of the element. The C3D8 element has six Gauss points. Therefore, the results obtained with C3D8 elements will be more numerically accurate than those obtained with the C3D8R element. Mesh seeding of the parts was done such that the number and thicknesses of elements across any two parts is the same at the interface. This approach offers flexibility in controlling meshing in this geometry as the cruciform model contains very fine and thick geometric features. It is difficult to obtain an acceptable mesh using global seeding. Subsequently, the meshes of individual parts were attached and the common nodes in the interface regions were merged. Fig. 3 shows a typical FEA mesh of the thin cruciform specimen. Note that the finite element model includes half thickness of the actual cruciform specimens. Two different FEA models were developed for the thin and thick cruciform specimens.

For the 1/8th symmetry model, appropriate symmetry boundary conditions were applied to each of the three symmetry planes. On each arm of the model, the nodes that are about 25 mm away in axial directions were assigned history-dependent displacement boundary conditions obtained from DIC measurements (see section 2 and Fig. 3). Note that all nodes along the depth were assigned the same boundary condition as those on the surface. On the X-arm, the nodes that have different Y coordinate values, but the same coordinate X value, are assigned different U displacement boundary conditions as obtained from DIC measurements. Such an approach is also followed for V displacement boundary condition on the Y-arm of the model for nodes that are located 25 mm away from the central node (but with varying X coordinate values). The ABAQUS implicit (or standard) solution algorithm was used [13].

Following completion of simulation, a path was defined along the diagonal using the same points used in the DIC analysis (see section 2.2 and Fig. 3). Computed strain and displacement data were mapped to 20 equidistant points along this diagonal for comparison with experimental measurements (discussed below in section 4). This mapping was done for each load point (squares in Fig. 2) corresponding to those when data were extracted from DIC measurements.

4. Results and Discussion

In this section FEA results will be compared with data obtained from experimental measurements. These data will be compared along the path as shown in Fig. 3. Such data are available for 5 points as shown in Fig. 2. In this paper, only results at the maximum load point will be discussed in detail. Consequently, experimental and simulated results extracted at point C in Fig. 2 for the thin specimen and point D in Fig. 2 for the thick specimen are discussed in this section. Also, all results are shown for the top surface of the model to be consistent with the DIC measurements. Overall, FEA results of displacement and strain fields

[1] Certain commercial software or materials are identified to describe a procedure or concept adequately. Such identification is not intended to imply recommendation, endorsement, or implication by NIST that the software or materials are necessarily the best available for the purpose.

show broad agreement with experimental data for all five points except for the first point for the thick sample. This is possibly due to elastic-plastic transient effects, and that the FEA model does not explicitly model the yield point behavior seen in Fig. 2 for thick specimen.

4.1 Displacement fields

Figure 5(a) and (b) show both experimental and computed U and V displacement fields in the thin specimen. Recall that there are 4 equivalent paths for which experimental data have been measured (e.g. 1 path for each quadrant, see Fig. 3). However, because of the symmetry used in the model, only one plot is shown for each ABAQUS model. Two sets of ABAQUS results are shown, one for reduced integration and one for regular elements. Figure 5 shows that the model predicts the displacement field accurately. There is variation in the experimental plots of V displacement profiles at the beginning of the path (e.g. near the X-arm), while the ABAQUS plots fall within the experimental curves. This could be the result of slight misalignment of the specimen to the X loading axis.

For the thick specimen, the results are shown in Fig. 6. Considerable variation is noticed among the experimental data. Overall, the computed displacement profiles are steeper than those observed experimentally. Both the computed U displacement and V displacement profile values are higher than the corresponding experimental values near the profile maxima. The reason behind this discrepancy is not

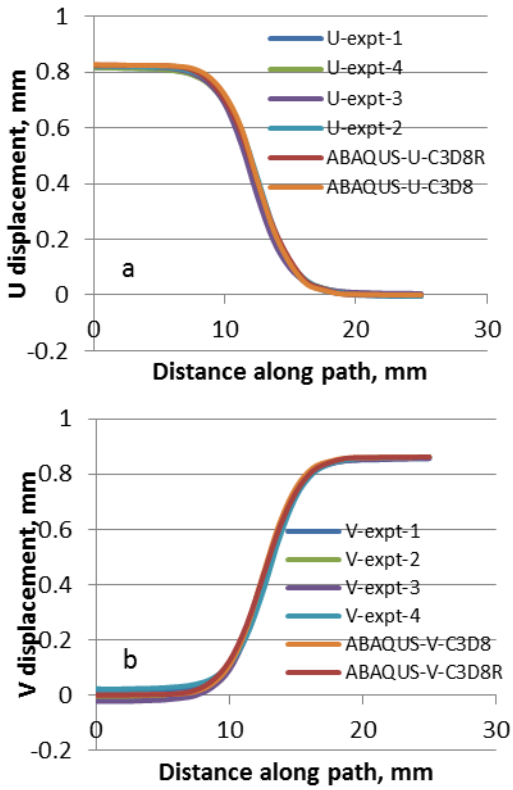

Fig. 5. Displacement along path for the thin specimen corresponding to the point C in Fig. 2. U-expt-1 to U-expt-4 show experimental U values along four equivalent paths; ABAQUS-U-C3D8R and ABAQUS-U-C3D8 are ABAQUS plots using C3D8R and C3D8 elements respectively. Similar naming convention is used for V displacement plots in Fig. 5(b).

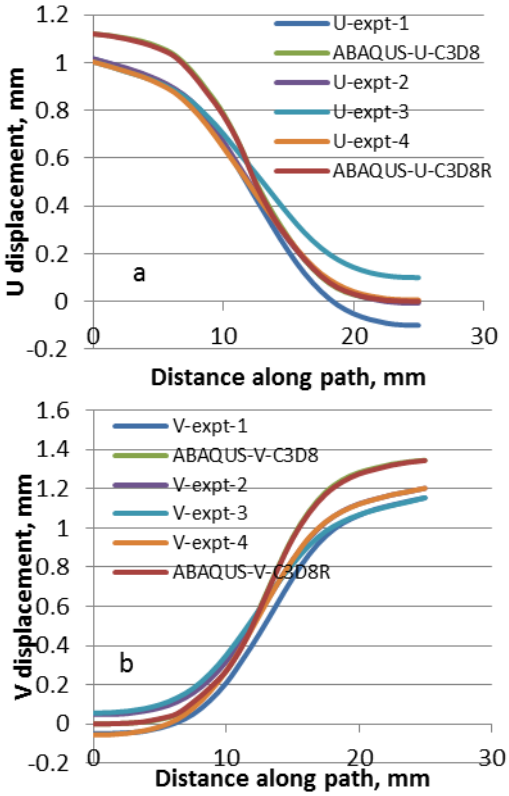

Fig. 6. Displacement along path for the thick specimen corresponding to the point D in Fig. 2. U-expt-1 to U-expt-4 show experimental U values along four equivalent paths; ABAQUS-U-C3D8R and ABAQUS-U-C3D8 are ABAQUS plots using C3D8R and C3D8 elements respectively. Similar naming convention is used for V displacement plots in Fig. 6(b).

clear. However, a full FEA model could have captured the material behavior more accurately because each arm would have proper boundary conditions corresponding to the actual experimental measurements. In the present case, average displacement data obtained in experimental measurements were used in the 1/8th symmetry model, thus averaging out any misalignment between the specimen and the loading axes. The thick specimen model shows slightly higher displacements than the thin specimen model, which one would expect by comparing the force-displacement curves in Fig. 2.

4.2 Strain fields

Figures 7(a), (b), and (c) show plots of normal strains in X, Y, and Z directions for the thin specimen corresponding to the point C in Fig. 2. The measured thickness strains were calculated assuming volume conservation, using $e_{zz} = -(e_{xx}+e_{yy})$. It is obvious from these plots that the ABAQUS simulations with C3D8 elements are in better agreement with experimental results compared to C3D8R elements. However, the modeled peak e_{zz} for C3D8 element exceeds those seen in experimental data. It is also noticed that the model predicts a slightly narrower width of the e_{zz} profile than the experimental results.

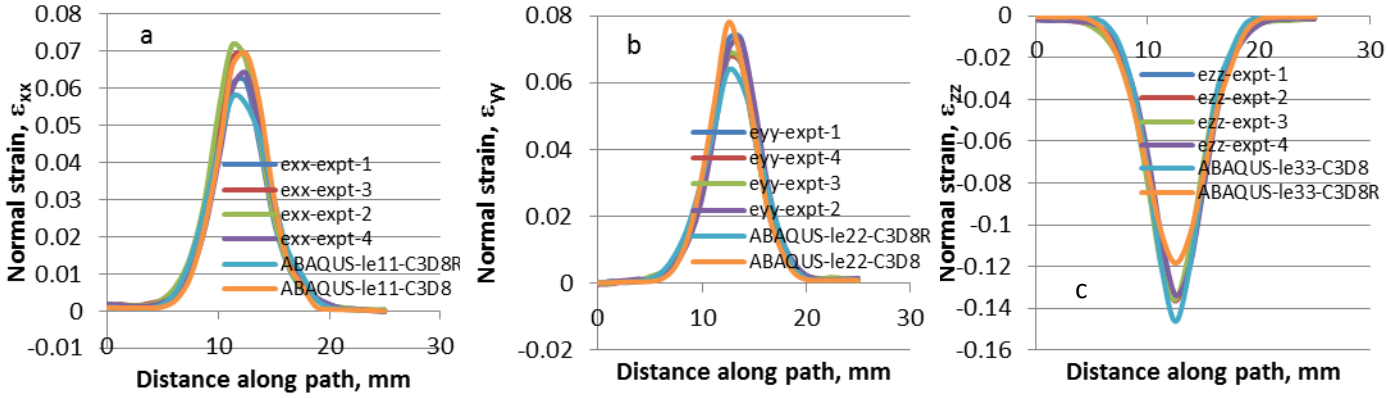

Fig. 7. X, Y, Z normal strains for the thin specimen corresponding to the point C in Fig. 2. exx-expt-1 to exx-expt-4 show experimental X-normal strains along four equivalent paths. ABAQUS-le11-C3D8R and ABAQUS-le11-C3D8 are ABAQUS X-normal strain plots using C3D8R and C3D8 elements respectively. Similar naming convention is used for Y and Z normal strain plots in Fig. 7(b) and 7(c).

For the thick specimen, the normal strain plots are shown in Fig. 8. Note that e_{xx} plots (Fig. 8(a)) show

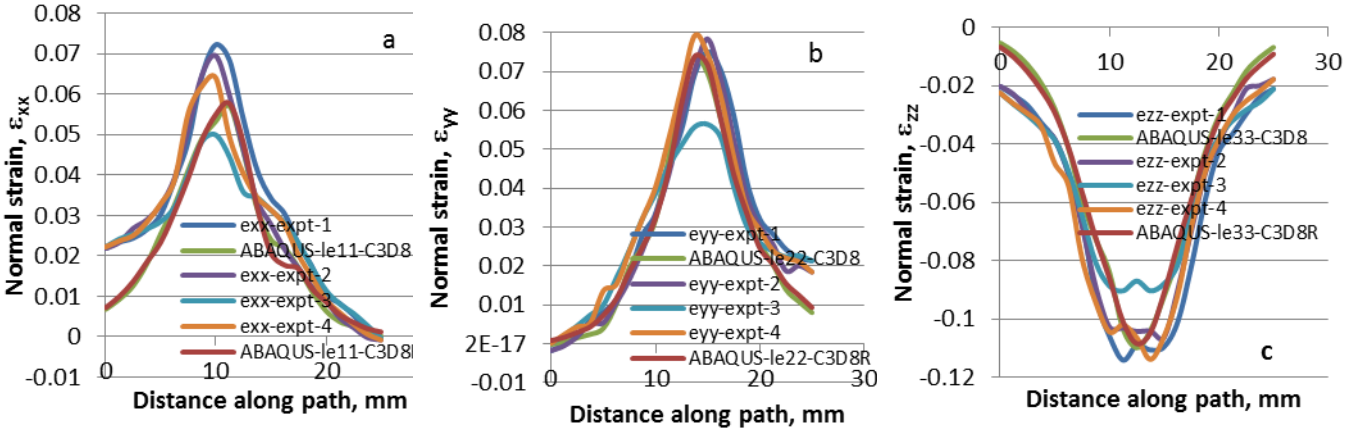

Fig. 8. X, Y, Z normal strains for the thick specimen corresponding to the point D in Fig. 2. exx-expt-1 to exx-expt-4 show experimental X-normal strains along four equivalent paths. ABAQUS-le11-C3D8R and ABAQUS-le11-C3D8 are ABAQUS X-normal strain plots using C3D8R and C3D8 elements respectively. Similar naming convention is used for Y and Z normal strain plots in Fig. 8(b) and 8(c).

that ABAQUS curves are within the experimental data except near the beginning of the path. Reverse trend is seen in for e_{yy} plots in Fig. 8(b), where the computed data deviate at the end of the path. This is consistent with the discrepancy seen in plots of displacement field shown in Fig. 6(a) and (b). Fig. 8(c) show that computed e_{zz} data deviate at both ends of the path but they are within the experimental bounds near the maximum point. This results in a sharper peak in the e_{zz} curves of the model than in the experimental curves.

4.3 Equivalent plastic strain

The von Mises equivalent strain plot obtained from DIC measurements is shown in Fig. 9. Note that this equivalent strain includes both elastic and plastic components, and extends to only about 0.3 mm of the surface edges. This experimental contour plot is compared with the von Mises equivalent plastic strain (PEEQ) available in ABAQUS. This comparison is justified since the expected contribution of elastic strain is very small.

Fig. 9 shows the measured equivalent field for the thin specimen, with largest value at the reentrant radius of about 0.38 and around 0.084 in the central region. Uniform equivalent strain is seen in the central pocket, which is also seen in the ABAQUS results in Fig. 10. The ABAQUS results show a value of 0.16 in the central pocket and a value of 0.3 at the outer edge of the reentrant corner. The model shows a slight decrease in strain along the diagonal from the reentrant radius to the peripheral region of the central pocket, where a value of about of 0.24 is obtained. Although the model does not show as thick a band of PEEQ of 0.3 along the diagonal from the reentrant radius to the peripheral region of the central pocket (as seen in experimental result in Fig. 9), it is intuitive that the failure initiation will probably start at the strain concentration at the base of the fillet from the thicker region into the thinner region. In fact, the experiment showed that the failure initiated at both the top left and bottom right of the pocket area at the base of the fillet radius, and these cracks propagated from the periphery to the center of the pocket.

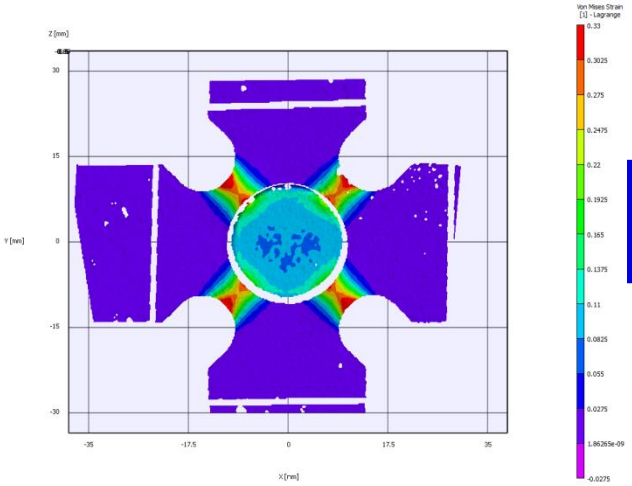

Fig. 9. Measured von Mises equivalent strain in the thin specimen at the maximum force point.

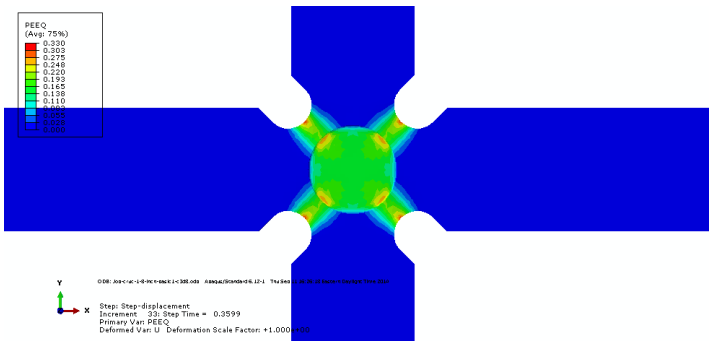

Fig. 10. ABAQUS computed von Mises equivalent plastic strain in the thin specimen at the maximum force point.

For the thick specimen, the measured von Mises equivalent strain contour plot is shown in Fig. 11. It is clear from this plot that strain values are higher along the diagonal, which is at 45° to the horizontal than the corresponding values along the diagonal that is at 135° to the horizontal. Along this diagonal (at 45° to the horizontal), equivalent strains of 0.27 or greater are seen at the peripheral region of the central pocket. A small band of 0.27 equivalent strain is seen near the outside edge of reentrant radius. ABAQUS computed results are shown in Fig. 12 (for the same load level). The ABAQUS strains range from 0.38 in

the central region of the pocket to about 0.25 near the peripheral region of the center pocket. An equivalent strain value of 0.24 is seen at the reentrant radius in the model. It is conceivable that failure will occur in the central pocket. In the actual experiment, the thick sample cracked in the central pocket region away from the periphery.

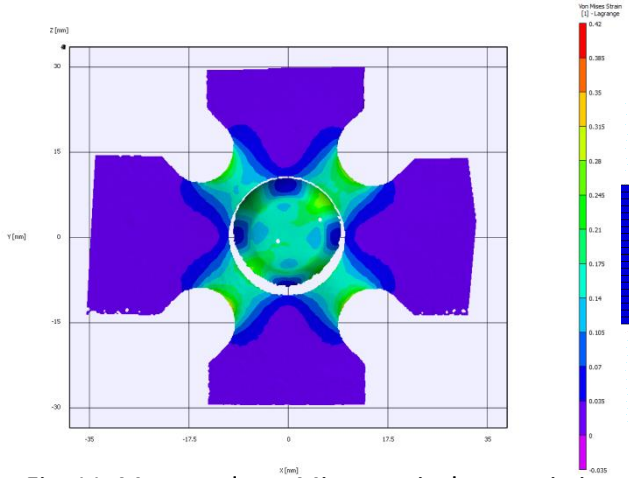

Fig. 11. Measured von Mises equivalent strain in the thick specimen at the maximum force point.

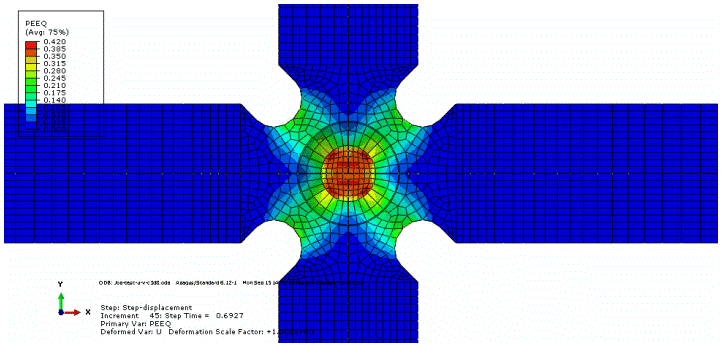

Fig. 12. ABAQUS computed von Mises equivalent plastic strain in the thick specimen at the maximum force point.

From the analysis of these two tests, it appears that that the thickness of the sample does have an influence on the eventual mode of failure. However, it is not possible to make a definite conclusion at this time because these two cruciform specimens were not made from the same material and did not have the same processing history.

5. Summary and future work

Finite element analyses of biaxial tensile tests using cruciform specimens were conducted using ABAQUS software. The numerical model uses constitutive material model data obtained from uniaxial tests. The FEA model employed history-dependent displacement boundary condition data that were obtained from in situ DIC measurement in the cruciform test frame. Overall, the numerical model showed reasonable agreement with experimental measurements when both displacement and strain fields were compared. Biaxial straining were seen in the central region of interest, as desired. The model predicts the path along which the eventual failure was seen in the experiment. ABAQUS results using C3D8 elements showed better agreement with experimental data in comparison with those obtained with the reduced C3D8R elements. This is especially true for the thin specimen.

Future work will include: (a) developing a full model of the specimen (ignoring mirror symmetry) and repeating the simulations using appropriate boundary condition data, (b) including anisotropic material properties and other relevant constitutive models, and (c) using ABAQUS in conjunction with an optimization software to develop the most optimum cruciform specimen design, (d) studying the influence of EDM on material properties in the thinned down central region, (e) investigating the influence of the presence of any discontinuities or defects on the overall deformation behavior, and (f) investigating the influence of sheet thickness on the mode of eventual specimen failure.

6. References

1. T. Foecke et al., “A method for direct measurement of multiaxial stress-strain curves in sheet metal”, *Metall.Mater Trans.* 38A (2007), 306–313.

2. M.A. Iadicola, T. Foecke, and S.W. Banovic, “Experimental observations of evolving yield loci in biaxially strained AA 5754-O”, *Int. J. Plasticity*, 24(11) (2008), 2084–2101.
3. W. Müller and K. Pöhlandt, “New experiments for determining yield loci of sheet metal”, *J. Mater. Process. Tech.*, 60 (1996), 643–648.
4. D.E. Green et al., “Experimental investigation of the biaxial behaviour of an aluminum sheet”, *Int. J. Plasticity*, 20 (2004), 1677–1706.
5. I.C. Noyan and J.B. Cohen, *Residual Stress: Measurement by Diffraction and Interpretation* (Springer-Verlag, 1987).
6. T. Kuwabara, A. Bael, and E. Iizuka, “Measurement and analysis of yield locus and work hardening characteristics of steel sheets with different r-values”, *Acta Mater* 50 (2002), 3717–3729.
7. E. Hoferlin et al., “The design of a biaxial tensile test and its use for the validation of crystallographic yield loci”, *Model. Simul. Mater. Sc.* 8 (2000), 423–433
8. T. Kuwabara, S. Ikeda, and K. Kuroda, “Measurement and analysis of differential work hardening in cold-rolled steel sheet under biaxial tension”, *J. Mater. Process. Tech.* 80-81 (1998), 517–523.
9. D. Banabic, “Anisotropy and formability of AA5182-0 aluminium alloy sheets”, *CIRP Annals-Manufacturing Technology* 53 (2004), 219–222.
10. F. Abu-Farha, L.G. Hector and M. Khraisheh, “Cruciform-shaped specimens for elevated temperature biaxial testing of lightweight materials”, JOM 61 (8) (2009), 48–56.
11. NIST Center for Automotive Lightweighting, http://www.nist.gov/lightweighting/.
12. M.A. Iadicola, A.A. Creuziger, and T. Foecke, “Advanced biaxial cruciform testing at the NIST Center for Automotive Lightweighting”, *SEM* (2013).
13. ABAQUS 12.2 software. Dassault Systemes. http://www.3ds.com/.
14. C.C. Tasan et al., “In-Plane biaxial loading of sheet metal until fracture”, *Society for Experimental Mechanics (SEM)*, (Orlando, FL: 2008).